Mathematical modelling of light propagation in the human eye

Adérito Araújo, Sílvia Barbeiro and Milene Santos

This review paper surveys the application of Maxwell's equations to simulate light propagation in the human eye, using discontinuous Galerkin methods for spatial discretisation. Understanding this process is crucial for medical imaging and the early diagnosis of eye diseases. Case studies involving corneal opacity, diabetic macular edema, and retinal elasticity demonstrate the importance of simulating this phenomenon considering realistic geometries and material properties. Specifically, these simulations provide valuable insight into how structural changes in the cornea and retina affect light scattering and transparency, offering a useful tool for non-invasive diagnosis. Curved anatomical features, such as structures of the eye, require accurate boundary representation to avoid loss of order of convergence of the numerical schemes. Highorder discontinuous Galerkin method combined with a polynomial reconstruction technique enable an appropriate enforcement of boundary conditions without relying on curved meshes.

1 Introduction

Light entering the human eye undergoes refraction and transformation as it passes through layered media with varying refractive indices, including the cornea, aqueous humour, lens, vitreous humour, and retina [17] (see Figure 1). These structures collectively focus and guide light toward the retina, where photoreceptor cells convert electromagnetic waves into neural signals for vision. Accurately modelling light propagation through these structures is essential not only for understanding the fundamental optics of vision, but also for improving diagnostic imaging techniques and uncovering biomarkers of disease.

Among modern ophthalmic imaging modalities, optical coherence tomography (OCT) has become a widely adopted standard in both research and clinical use. Since its introduction in the 1990s [15], OCT has revolutionised the non-invasive evaluation of the retina by enabling cross-sectional imaging with high axial resolution. It operates on the principle of low-coherence interferometry: a beam of light is directed into the tissue and backscattered photons are

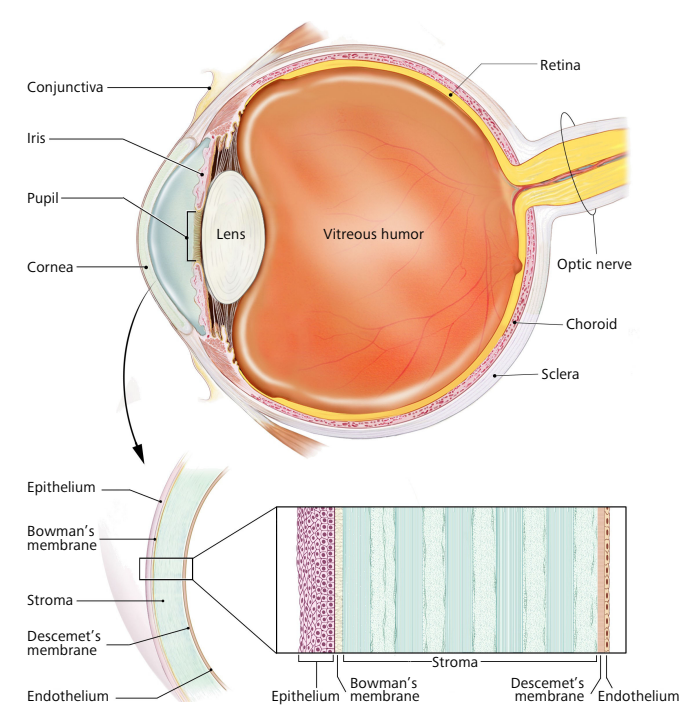


Figure 1. Structure of the human eye. (National Eye Institute, CC BY 2.0)

captured to generate high-resolution cross-sectional images of the tissue. As light propagates through tissue, scattering occurs at refractive index discontinuities. The magnitude of the backscattered light is influenced by factors such as the size and shape of the scatterers, the incident wavelength, and local optical heterogeneity. The OCT signal at each point is captured in an A-scan, and multiple A-scans collected laterally form a B-scan; three-dimensional imaging is obtained by compiling a stack of B-scans across the azimuthal plane (see Figure 2 and Figure 3).

OCT plays a central role in the diagnosis, staging, and monitoring of major ocular diseases such as diabetic macular edema (DME), age-related macular degeneration (AMD), and glaucoma [12]. Beyond ophthalmology, OCT has also emerged as a valuable tool in neurology, with retinal changes being increasingly recognised as biomarkers of central nervous system disorders, including multiple

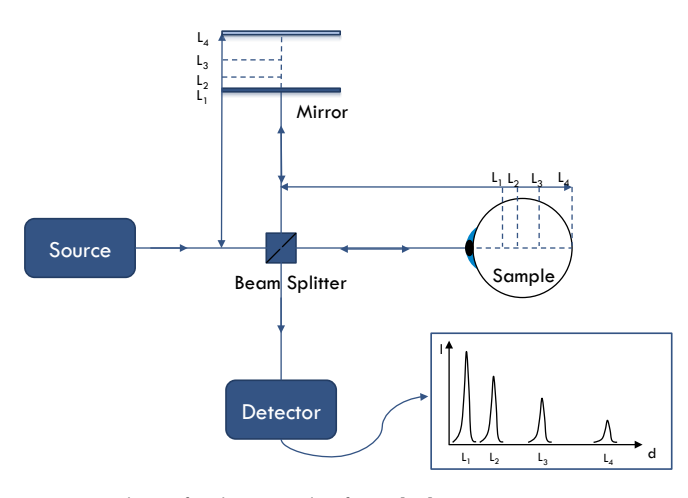


Figure 2. Scheme for the principle of OCT [29].

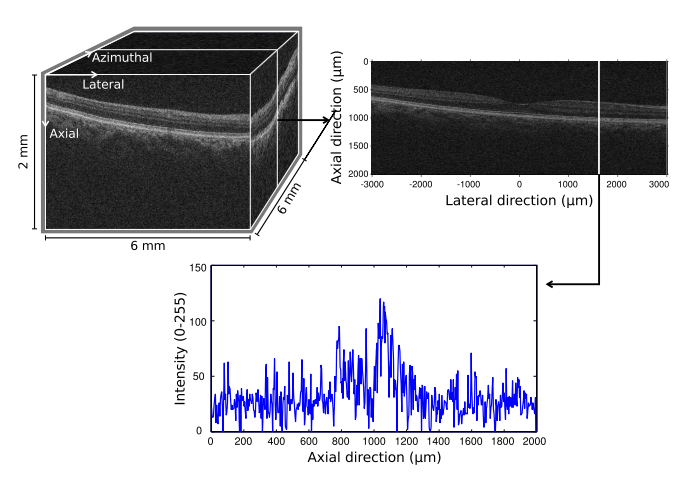


Figure 3. Example of an OCT volume (top left), B-scan (top right) and A-scan (bottom) of a human retina [9].

sclerosis, diabetic retinopathy, Parkinson's disease, and Alzheimer's disease [7, 24, 27]. However, despite its widespread use, OCT has intrinsic limitations. The technique is primarily sensitive to backscattered light intensity and does not provide direct access to sub-cellular features or to the underlying optical parameters (e.g., refractive index distribution, anisotropy) that drive contrast formation in scattering tissues.

Understanding how microscopic changes, such as extracellular fluid accumulation, cell swelling or microstructure organisation, affect the macroscopic OCT signal is therefore a crucial step towards improving the sensitivity and specificity of OCT-based diagnoses. Many early pathological changes in both ocular and neurological diseases are subtle and occur at scales below the resolution of OCT. Accurately linking these microscopic changes to OCT signal patterns requires detailed biophysical models of light propagation in the eye, capable of resolving scattering and interference phenomena in realistic anatomical geometries.

Maxwell's equations provide the most complete and physically consistent framework for modelling electromagnetic wave propagation in biological tissues. However, their numerical solution in full three-dimensional ocular domains presents significant challenges: the wavelength of light is several orders of magnitude smaller than the overall domain size; the anatomical structures involve curved, multilayered boundaries with sharp optical property contrasts; and the resulting wave fields are highly oscillatory. To address these complexities, we employ high-order discontinuous Galerkin (DG) methods for spatial discretisation. DG methods combine the geometric flexibility of finite elements with the high-order accuracy and local conservation properties of spectral methods, making them especially well suited for simulating timedomain wave propagation in heterogeneous biological media [14]. The use of low-storage Runge-Kutta time integrators further enables long-time simulations while preserving computational efficiency [31].

Anatomical accuracy is central to our modelling approach. Optical phenomena such as forward and multiple scattering, or subtle angular dependencies of the backscattered signal, can be strongly influenced by small geometric features. Errors in representing curved interfaces, such as the corneal surface or retinal layers, can lead to misleading conclusions. While high-order curved meshes offer one approach to improving geometric accuracy, they often introduce significant meshing and computational overhead. To address these challenges, we adopt a polynomial reconstruction approach that applies boundary conditions directly on smooth anatomical surfaces, maintaining high-order accuracy without requiring curved mesh elements. This enables precise modelling of the optical properties of the eye, including complex light paths and tissue-specific scattering behaviours.

In the following sections, we present an electromagnetic model of the human eye, considering both scattered-field and total-field configurations. We detail the DG spatial discretisation, the high-order time integration scheme, and the implementation of realistic anatomical geometries. Finally, we apply our methodology to three clinically motivated scenarios: changes in corneal transparency, light scattering in retinal layers affected by DME, and elastic-wave propagation relevant to optical coherence elastography. These case studies illustrate how high-order modelling can enhance the interpretation of OCT data, support early diagnosis, and contribute to a deeper understanding of disease mechanisms at the microstructural level.

2 Maxwell's equations

Maxwell's equations describe how electromagnetic waves propagate in a medium and are essential for modelling light transmission through the eye [18]. The electromagnetic field involves four vector

fields: the electric field E, magnetic field H, electric flux density D, and magnetic flux density B. Constitutive relations link these fields via D = ε E and B = μ H, where ε is the permittivity tensor and μ the permeability. In isotropic media, $\varepsilon = \varepsilon I$ with scalar ε , and $\mu > 0$ is typically close to the vacuum permeability in biological tissues. These parameters determine the refractive index, wave speed $c = 1/\sqrt{\varepsilon\mu}$, and impedance $Z = \sqrt{\mu/\varepsilon}$, all critical for accurate modelling of light propagation through the eye's heterogeneous structures.

Assuming zero charge density and zero current density, and using the constitutive relations, Maxwell's equations in a source-free isotropic medium can be written as

$$\varepsilon \frac{\partial \mathsf{E}}{\partial t} = \nabla \times \mathsf{H},\tag{1}$$

$$\mu \frac{\partial \mathbf{H}}{\partial t} = -\nabla \times \mathbf{E},\tag{2}$$

where $\nabla \times$ denotes the curl operator, $\mathbf{E} = (E_x, E_y, E_z)^{\mathsf{T}}$ and $\mathbf{H} = (H_x, H_y, H_z)^{\mathsf{T}}$.

In the context of light propagation in the eye, the transverse electric (TE) mode of Maxwell's equations provides a simplified yet physically relevant representation of electromagnetic wave behaviour. In TE mode, the magnetic field is assumed to be polarised perpendicular to the plane of propagation (commonly taken as the xy-plane). So the electric field lies entirely in the transverse plane and has two components of interest, usually denoted by E_x and E_y , while the magnetic field has a non-zero component in the direction of propagation, usually denoted by H_z . This simplification suits many biological optics applications, including the eye, where light is often linearly or partially polarised with the electric field primarily oriented in the plane defined by ocular structures. The properties of tissues such as the corneal stroma and retina strongly influence these in-plane fields [21]. The TE mode also enables realistic simulation of polarisation-dependent phenomena, such as scattering and absorption, which are crucial for advanced imaging techniques like optical coherence tomography and polarimetry [12]. From a computational standpoint, the TE mode reduces Maxwell's equations to a coupled system involving only three components, namely E_x , E_{ν} and H_{z} , facilitating efficient numerical implementations. In a 2D TE mode setting, time-domain Maxwell's equations (1)–(2) can be expressed as

$$\varepsilon \frac{\partial E_x}{\partial t} = \frac{\partial H_z}{\partial v},\tag{3}$$

$$\varepsilon \frac{\partial E_y}{\partial t} = -\frac{\partial H_z}{\partial x},\tag{4}$$

$$\mu \frac{\partial H_z}{\partial t} = -\left(\frac{\partial E_y}{\partial x} - \frac{\partial E_x}{\partial y}\right). \tag{5}$$

Thus, the TE mode offers an effective balance between physical realism and numerical tractability for modelling light propagation in the eye. It accurately represents the in-plane electric field interactions with ocular tissues while simplifying the electromagnetic problem, making it a preferred choice in many optical analyses of the eve.

A comprehensive description of an electromagnetic problem should include both the governing differential equations and the corresponding boundary conditions. Since simulations are performed within a finite domain Ω with boundary $\partial\Omega$, it is essential to implement boundary conditions that accurately represent the behaviour of waves exiting the domain. Silver–Müller absorbing boundary conditions simulate open boundaries that allow outgoing waves to exit the domain without reflection. On a boundary with outward unit normal vector $\mathbf{n} = [n_x, n_y]^{\mathsf{T}}$, they are given by

$$\mathbf{n} \times \mathbf{E} = Z\mathbf{n} \times (\mathbf{H} \times \mathbf{n})$$
 on $\partial \Omega$.

These conditions are designed to replicate the effect of an open domain by minimising spurious reflections at the computational boundary. Derived from plane wave solutions of Maxwell's equations, they are particularly well suited for problems in which electromagnetic waves radiate outward from the domain [18].

3 Discontinuous Galerkin method

Discontinuous Galerkin (DG) methods are a class of finite element methods that combine the advantages of finite volume and finite element schemes [14]. They are particularly suitable for solving hyperbolic partial differential equations, such as Maxwell's equations, because of their ability to handle complex geometries, adaptivity, and high-order accuracy.

Let $\mathbf{U} = (E_x, E_y, H_z)^{\mathsf{T}}$ denote the vector of unknowns. The system (3)–(5) can be written in conservation form

$$Q\frac{\partial U}{\partial t} + \nabla \cdot F(U) = 0, \tag{6}$$

where $\nabla \cdot$ denotes the divergence operator, and the flux tensor F(U) and the material matrix Q are defined by

$$F(U) = \begin{bmatrix} 0 & -H_z \\ H_z & 0 \\ E_y & -E_x \end{bmatrix}, \quad Q = \begin{bmatrix} \varepsilon & 0 \\ 0 & \mu \end{bmatrix}.$$

The domain Ω is meshed with K non-overlapping elements T^k , k=1,...,K, leading to an approximate computational domain $\Omega_h = \bigcup_{k=1}^K T^k$. We seek a weak solution \mathbf{U}_h by requiring the residuals to vanish in the following way

$$\int_{\Omega_h} \mathbf{Q} \frac{\partial \mathbf{U}_h}{\partial t} \cdot \phi \, d\mathbf{x} + \int_{\Omega_h} \nabla \cdot \mathbf{F}(\mathbf{U}_h) \cdot \phi \, d\mathbf{x} = 0,$$

where ϕ is a test function from a discontinuous (piecewise polynomial) finite element space. Next, we employ one integration

by parts and replace the flux \hat{F} by a numerical flux \hat{F} . Applying integration by parts again yields

$$\sum_{k=1}^{K} \int_{T^{k}} \left(Q \frac{\partial U_{h}}{\partial t} dx + \nabla \cdot F(U_{h}) \right) \cdot \phi dx$$

$$= \sum_{k=1}^{K} \int_{\partial T^{k}} \mathbf{n} \cdot (\mathbf{F} - \hat{\mathbf{F}}) \cdot \phi ds,$$

where **n** is the outward unit normal vector of the contour.

Numerical fluxes are used in DG methods to manage discontinuities at element interfaces. A common choice is the upwind flux, which incorporates the wave propagation direction and ensures numerical stability. Alternatively, central fluxes with penalty terms may be employed. Introducing the notation for jumps of fields $\llbracket u \rrbracket = u^- - u^+$, where - refers to the local cell and + refers to the neighbouring one, we define the upwind flux as $\llbracket 14,19 \rrbracket$

$$\mathbf{n} \cdot (\mathbf{F} - \hat{\mathbf{F}}) = \begin{pmatrix} \frac{-n_y}{Z^+ + Z^-} (Z^+ \llbracket H_{hz} \rrbracket - (n_x \llbracket E_{hy} \rrbracket - n_y \llbracket E_{hx} \rrbracket)) \\ \frac{n_x}{Z^+ + Z^-} (Z^+ \llbracket H_{hz} \rrbracket - (n_x \llbracket E_{hy} \rrbracket - n_y \llbracket E_{hx} \rrbracket)) \\ \frac{1}{Y^+ + Y^-} (Y^+ (n_x \llbracket E_{hy} \rrbracket - n_y \llbracket E_{hx} \rrbracket) - \llbracket H_{hz} \rrbracket) \end{pmatrix},$$

with impedance $Z^{\pm}=\sqrt{\mu^{\pm}/\varepsilon^{\pm}}$ and conductance $Y^{\pm}=1/Z^{\pm}$. These choices ensure that energy transmission and reflection at interfaces are physically accurate. These flux expressions help maintain consistency, stability, and physical fidelity of the numerical scheme. For Silver–Müller absorbing boundary conditions, we consider at the outer boundary

$$E_{hy}^{+}n_{x}-E_{hx}^{+}n_{y}=Z^{-}H_{hz}^{+}$$

which is equivalent to considering $\llbracket E_{hx} \rrbracket = E_{hx}^-$, $\llbracket E_{hy} \rrbracket = E_{hy}^-$ and $\llbracket H_{hz} \rrbracket = H_{hz}^-$. To complete the evaluation of fluxes at boundary edges, we mention that the material properties at the boundary are set as $Z^+ = Z^-$ and $Y^+ = Y^-$.

4 Time integration

The system of ordinary differential equations resulting from the spatial discretisation of Maxwell's equations using the DG method takes on the form

$$\frac{d\mathbf{U}_{\mathsf{h}}}{dt} = \mathcal{L}_{\mathsf{h}}(\mathbf{U}_{\mathsf{h}}),$$

where $\mathcal{L}_{h}(U_{h})$ includes the contributions from element integrals, numerical fluxes and the material matrix.

Explicit low-storage Runge–Kutta (LSRK) methods are particularly well suited for time integration in wave propagation problems due to their balance of efficiency, accuracy, and stability. Unlike standard Runge–Kutta schemes that require multiple storage vectors for intermediate stages, LSRK methods reuse just a few vectors – typically two – through recursive updates. This leads to significantly reduced memory usage, an important feature in large-scale simulations.

LSRK methods can achieve high-order temporal accuracy, typically fourth or fifth order, while maintaining favourable stability properties for hyperbolic systems. Their explicit formulation makes them easy to implement and naturally suited for parallel computation. Although there are several ways to implement LSRK methods, we adopt the formulation introduced by Williamson [31], which uses only two vectors – one for the solution and one for the residual – and is well suited to large-scale DG simulations. The method proceeds as follows:

$$\mathbf{U}^{(0)} = \mathbf{U}_{h}^{n}, \quad \mathbf{R}^{(0)} = \mathbf{0},$$

$$\mathbf{R}^{(i)} = \alpha_{i} \mathbf{R}^{(i-1)} + \Delta t \, \mathcal{L}_{h} (\mathbf{U}^{(i-1)}),$$

$$\mathbf{U}^{(i)} = \mathbf{U}^{(i-1)} + \beta_{i} \mathbf{R}^{(i)}, \quad i = 1, ..., s,$$

$$\mathbf{U}_{h}^{n+1} = \mathbf{U}^{(s)}.$$

where a_i and θ_i are method-specific coefficients chosen to achieve high-order accuracy and favourable stability properties, Δt is the time step, and s is the number of stages. The method reuses the vectors \mathbf{U} and \mathbf{R} at each stage, thus achieving low memory consumption. In this work, we consider the L(14,4) scheme by Niegemann, Diehl, and Busch [22], a method of 14 stages and order of accuracy 4. These methods were designed to minimise memory usage while maximising stability, making them particularly well suited for high-order spatial discretisations such as discontinuous Galerkin methods applied to hyperbolic problems.

An alternative to LSRK methods for time integration of Maxwell's equations is the Leapfrog scheme, which is commonly used due to its explicitness, simplicity, and time centred structure that matches the staggered nature of Maxwell's equations [3, 4]. In the Leapfrog scheme, the electric field $\mathbf{E} = (E_x, E_y)$ and magnetic field H_z are updated at staggered time levels. The electric fields E_x , E_y are computed at integer time steps $t^n = n\Delta t$ and the magnetic field H_z is computed at half-time steps $t^{n+1/2} = (n+1/2)\Delta t$. This time-centred structure is second-order accurate and conditionally stable under a CFL condition, which imposes a bound on the time step Δt depending on the mesh size h and the wave speed. Theoretical results on stability and convergence may be found in [3, 4]. The Leapfrog method is particularly attractive for long-time simulations due to its low computational cost and symplectic nature, preserving energy in non-dissipative systems. However, it requires care when dealing with complex geometries, boundary conditions, and variable material properties, especially when combined with DG spatial discretisations.

5 Case studies

Early detection of eye diseases is essential for effective treatment and preserving vision. Conditions such as corneal disorders and diabetic macular edema often involve subtle alterations of the microstructure of the tissue. Optical coherence tomography (OCT)

and optical coherence elastography (OCE) are two non-invasive imaging techniques used in ophthalmology to detect abnormalities in the eye. This section presents three case studies that perform simulations based on Maxwell's equations to model the effect of these changes on OCT/OCE signals.

5.1 Corneal transparency problem

The cornea is the transparent outer layer of the eye, and it plays a key role in directing and focusing light toward the retina. It is composed of five layers: the epithelium, Bowman's layer, the stroma, Descemet's membrane, and the endothelium (see Figure 1). Under healthy conditions, these layers remain thin and well structured, minimising light scattering. However, pathological modifications to any of these layers can disrupt this structure, leading to increased light scattering and a loss of corneal transparency [20]. Among the five layers, the stroma corresponds to nearly 90% of the total corneal thickness and is mainly composed of collagen fibrils with uniform diameters that are further gathered into collagen lamellae. Among other functions, these collagen fibrils are responsible for maintaining the structural regularity that supports transparency [21]. Specifically, what is maintained is the uniformity of the diameters of the collagen fibrils and the distances between adjacent collagen fibrils. Alterations in either of these properties may result in increased light scattering, compromising corneal transparency.

Corneal opacity problem is a common issue in vision diseases, particularly for ageing population, while decreased visual acuity is associated with a reduced quality of life and life expectancy. Diagnostic is based on cornea analysis using OCT.

Ageing of the ocular surface and corneal tissues causes major eye diseases and results in substantial costs in both medical and social terms. Furthermore, often corneal edema occurs after surgery for treating cataracts is performed. Understanding the mechanisms of transparency loss requires understanding the structural bases of corneal transparency itself, which ensure minimal scattering of visible light. Scattering takes place when an incident light wave encounters fluctuations in the refractive index of a material, characterised by the matrix of collagen fibrils. Modelling and simulating the cornea transparency loss is a critical digital tool to measure and prevent possible illnesses.

Results in [2] illustrate that an increase in the diameter of some fibrils causes an increase in backscattering. Therein, the problem was studied considering a two-dimensional model of backscattered light in two different scenarios (healthy and pathological).

To simulate light scattering in the cornea, the scattered field formulation for the transverse electric (TE) mode was adopted. This involves decomposing the total electromagnetic field into two components: the incident field $U^{\dagger} = (E_X^{\dagger}, E_Y^{\dagger}, H_Z^{\dagger})^{\mathsf{T}}$, which represents the

wave propagating in the absence of scatterers, and the scattered field $U^s = (E_x^s, E_y^s, H_z^s)^T$, which accounts for the perturbation caused by the inhomogeneities. Thus, the total field is expressed as the sum of the incident and scattered components.

Assuming the incident field satisfies the Maxwell equations (3)–(5) with relative permittivity ε_0 and permeability $\mu_0=\mu$ corresponding to the background (scatterer-free) medium, we substitute this decomposition into equation (3)–(5). This leads to the scattered field formulation, which isolates the effect of the scattering medium on the wave propagation:

$$\varepsilon \frac{\partial E_x^s}{\partial t} = \frac{\partial H_z^s}{\partial y} + (\varepsilon_0 - \varepsilon) \frac{\partial E_x^i}{\partial t},\tag{7}$$

$$\varepsilon \frac{\partial E_y^s}{\partial t} = -\frac{\partial H_z^s}{\partial x} + (\varepsilon_0 - \varepsilon) \frac{\partial E_y^i}{\partial t},$$
 (8)

$$\mu \frac{\partial H_z^s}{\partial t} = \frac{\partial E_x^s}{\partial y} - \frac{\partial E_y^s}{\partial x}.$$
 (9)

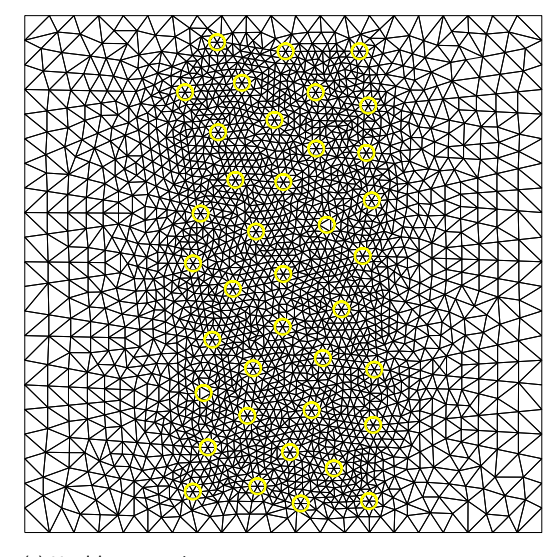
For a computational (dimensionless) domain we took $\Omega_h=[-1,1]^2$ with circles that stand for the collagen fibrils of the cornea. In the healthy scenario, we considered that the diameter of each fibril is 31 nm. In the pathological situation, the positions of the fibrils were kept and eight fibrils were randomly chosen to have doubled diameter. For the numerical simulations, the magnetic permeability was set to $\mu=1$, the electric permittivity of the free space to $\varepsilon_0=1.365^2$ and ε is such that

$$\varepsilon(x,y) = \begin{cases} 1.411^2, & (x,y) \in \mathcal{F}, \ (x,y) \in \mathcal{F}', \\ 1.365^2, & (x,y) \in \Omega \setminus \mathcal{F}, \ (x,y) \in \Omega \setminus \mathcal{F}', \end{cases}$$

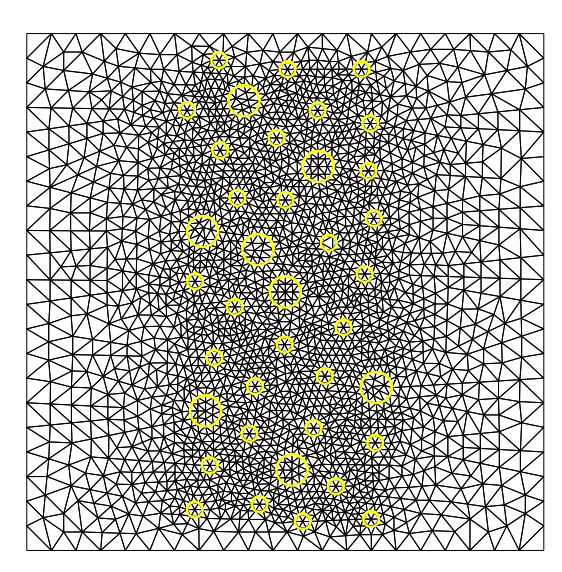
where \mathcal{F} denotes the union of circles that model healthy collagen fibrils and \mathcal{F}' represents the pathological situation. The scattered field formulation is completed with Silver–Müller absorbing boundary conditions and initial conditions defined by $U^s(x,y,0)=0$ and $U^i(x,y,0)=(0,\cos(10(x-t)),0)^{\top}$.

The spatial discretisation is done on meshes defined in Figure 4 using the DG method. Note that, when considering the scattered field formulation (7)–(9), the conservation form (6) would have an additional term $G(U^i)$ that results from the incident field. The low-storage explicit Runge–Kutta method, L(14,4), is applied for time integration with step $\Delta t = 10^{-3}$, respecting the stability constrains [5]. The intensity of the scattered electric field, $I^s = \sqrt{(E_X^s)^2 + (E_Y^s)^2}$, is represented in Figure 5 where the solution was approximated by polynomials of order N = 4 and plotted for different values of simulation time T.

As one can see in Figure 5, the planar characteristic of the wavefront is significantly lost in the situation where we double the diameter of 20% of the stromal fibres. One can also observe an increase in backscattering in the case where the organisation of the fibrils is not uniform, which subsequently leads to corneal swelling and a loss of transparency, as predicted in [21].



(a) Healthy scenario.



(b) Pathological scenario.

Figure 4. Spatial meshes for the healthy and pathological scenarios. The mesh in (a) is composed of K = 5072 elements, and the mesh in (b) counts K = 4972 elements [2].

5.2 Simulation of diabetic macular edema changes on optical coherence tomography data

Diabetes mellitus is one of the most prevalent diseases in developed countries. According to the World Health Organization (WHO), approximately 74 million adults in the WHO European Region are living with diabetes, with prevalence rates of 11.9% among men and 10.9% among women [32]. This marks a significant increase from earlier estimates and underscores the growing public health challenges posed by diabetes in Europe. Projections indicate that by 2045 one in ten adults in the region will live with diabetes [16].

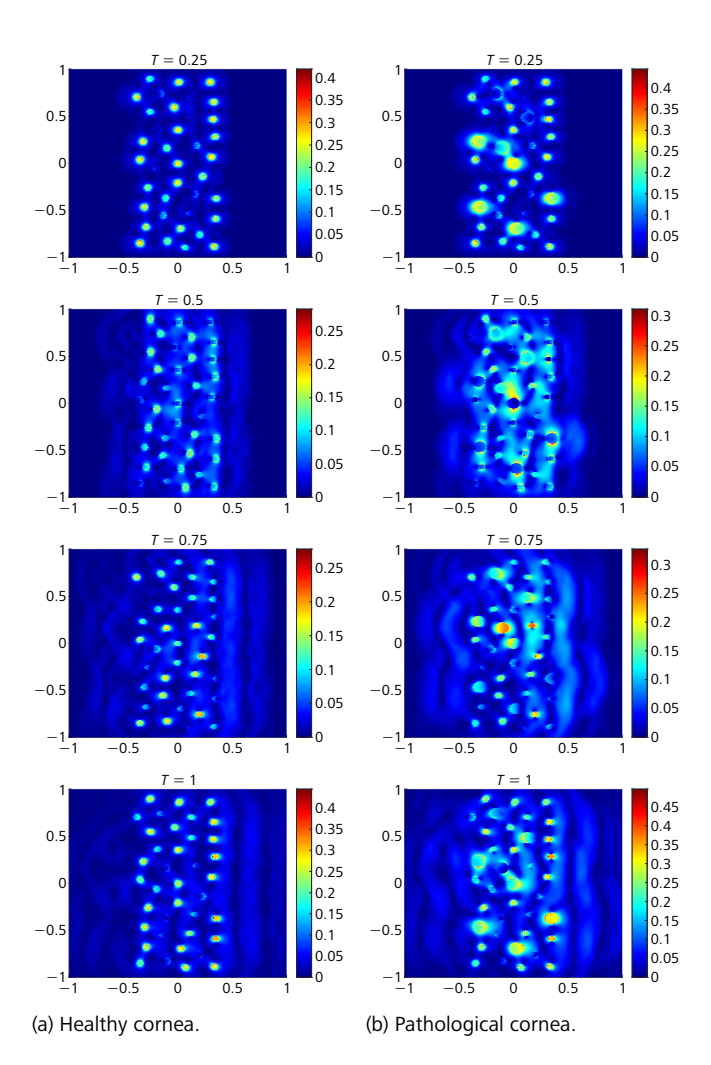


Figure 5. Scattered electric field intensity [2].

A major complication in diabetes is diabetic macular edema, one of the leading causes of visual impairment among diabetic patients [8]. DME is defined as an increase in retinal thickness due to fluid accumulation, which may occur intra- or extracellularly. In intracellular edema, cells retain excess fluid, becoming enlarged, whereas extracellular edema results from the accumulation of fluid outside cells, often due to a breakdown in the blood-retinal barrier [10]. Differentiating the type and severity of DME in its early stages is often challenging.

OCT is a widely used imaging technique that provides highresolution views of retinal structure in vivo (Figure 6), making it essential for diagnosing and monitoring DME. However, standard OCT lacks the ability to directly capture microscopic changes at the cellular level, particularly the morphological alterations linked to intracellular and extracellular edema. Understanding how these microscopic features influence the macroscopic OCT signal is therefore crucial. To address this, Correia et al. [9] developed a hybrid

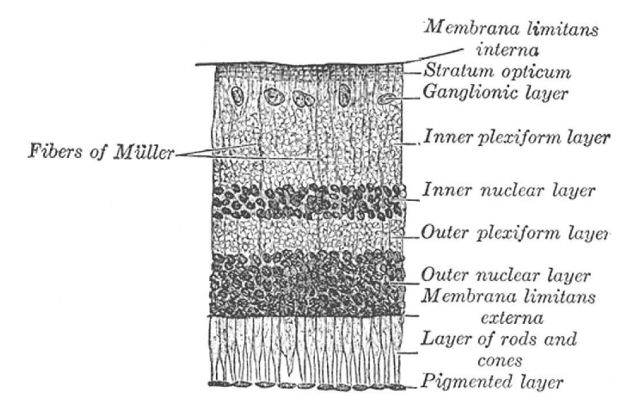


Figure 6. Section of the retina. From Henry Gray: Anatomy of the Human Body (Philadelphia: Lea & Febiger, 1918). (In public domain at bartleby.com.¹)

simulation framework that integrates physical models of light propagation with biologically-informed retinal representations, focusing on a 3D optical model of the outer nuclear layer (ONL), a region consistently affected in DME and amenable to modelling via spherical scatterers.

Various methods have been proposed to describe the interaction of light with retinal tissues. Most are based on single-scattering theory [28], which is insufficient to fully capture the structural complexity of the retina. The Mie solution to the equations in question is among the most widely used techniques for modelling tissue scattering at the cellular level [17]. However, Mie theory is limited to scattering by a single homogeneous sphere, restricting its applicability to scatterers of different shapes or aggregates. This limitation is partially overcome by the generalized multiparticle Mie (GMM) theory introduced in [33], which extends Mie's solution to account for multiple scattering in aggregates of spheres and enables more accurate modelling of biological tissue. Nevertheless, GMM is still confined to spherical structures.

More complex models need to be used when considering scatterers of arbitrary shapes. The finite-difference time-domain method is a numerical technique used to solve the Maxwell equations in the time domain that has been applied to a wide range of electromagnetic problems, including light scattering from biological cells [11,30]. In [25], Maxwell's equations were solved on a small 3D ONL domain using the DG method, coupled with a fourth-order, 14-stage low-storage Runge–Kutta integrator. Silver–Müller boundary conditions were applied to suppress spurious reflections. The model was validated against Mie's theory using identical parameters, showing good agreement with errors of 0.37% for the scattering anisotropy and 0.06% for the scattering cross-section [25].

An algorithm to simulate A-scans was also developed. A sinusoidal plane wave propagating in the z-direction excites the domain,

and the DG model computes fields around a single spherical scatterer representing an ONL nucleus. Anisotropy (g) and scattering cross-section (σ_s) are obtained from the far-field scattering pattern in spherical coordinates. A Monte Carlo simulation then launches 10^9 photons, simulating distances between interactions (using σ_s) and angular deflections (using g). Photon paths reaching a 15 μ m radius detector within a 5° acceptance cone are recorded. Comparing simulated and experimental A-scans allows identification of parameter sets that best reproduce the observed data.

The tool was applied to OCT scans (Cirrus HD-OCT, Carl Zeiss Meditec) collected from healthy subjects and two DME patient groups: DME I (increased ONL thickness) and DME II (no apparent ONL change). Literature-based parameters (Table 1) were used for healthy tissue, while parameters d (nucleus diameter in DME I) and ρ (nucleus density in DME II) were adjusted to fit the measured A-scans [9].

Group	Nuclei diameter (μm)	Nuclei density (nuclei/µm³)	Nuclei RI (at 870 nm)	Medium RI (at 870 nm)
Healthy	7.0	0.002	1.39	1.35
DME I	d	0.002	1.39	1.35
DME II	7.0	ρ	1.39	1.35

Table 1. Properties of the medium used in Monte Carlo simulations [9].

For each group, the ONL was segmented and B-scans were aligned to the upper ONL boundary. Mean B-scans and A-scans were computed and normalised to the maximum intensity at the retinal pigmented epithelium. Final A-scans were cropped to the minimum ONL thickness observed to ensure consistency (Figure 7).

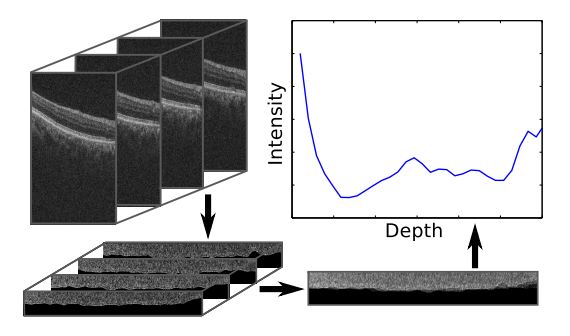


Figure 7. OCT processing algorithm (counterclockwise from upper left corner). The ONL of a group's B-scans are segmented and aligned to their upper boundary. The segmented B-scans are averaged to produce a demonstrative B-scan. The A-scans are averaged to obtain an A-scan that fully describes the group [9].

¹ https://www.bartleby.com/lit-hub/anatomy-of-the-human-body

It was observed that DME group I (Figure 8(a)) consistently exhibits a stronger intensity signal compared to healthy controls. To replicate this condition in simulation, it was necessary to increase the nuclei diameter by 14% relative to the healthy state. In [9], the data for DME group I were successfully reproduced by increasing the nuclear radius d from 7.0 μ m to 8.0 μ m, while keeping all other parameters unchanged.

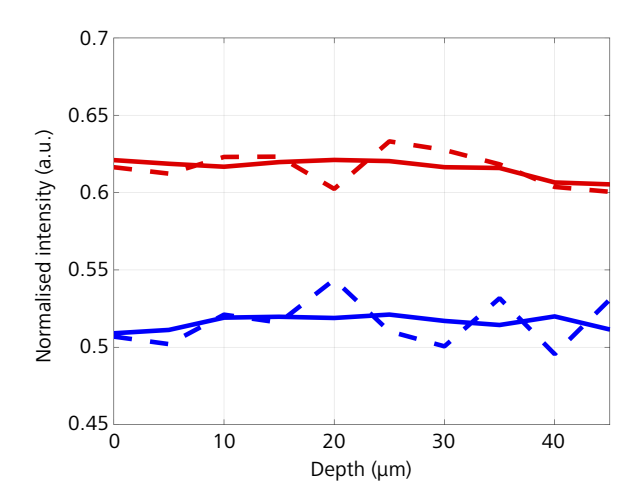
In contrast, DME group II (Figure 8(b)) shows a reduced backs-cattered signal compared to healthy tissue, which is consistent with theoretical expectations. A thicker layer containing the same number of nuclei should result in a lower backscattering signal due to the reduced density of scatterers. In [9], this behaviour was replicated by reducing the simulated nuclei density by 40%. Specifically, the density ρ was decreased from 0.002 μ m⁻³ to 0.0012 μ m⁻³, based on the assumption that the number of nuclei remains constant while the volume of the ONL increases. This adjustment reflects the observed ONL thickness increase from 70 μ m to 117.2 μ m.

The results reported in [9] support the hypothesis that the two types of edema, cytotoxic (intracellular) and vasogenic (extracellular), can be distinguished through OCT signal characteristics. In the case of DME group I, the increased OCT signal is best explained by an enlargement of the nuclei, which is compatible with intracellular swelling. While alternative mechanisms, such as changes in nuclear radius or the refractive index of the surrounding medium, could also affect the signal, this preliminary study restricted the analysis to physiological alterations consistent with known biological behaviour.

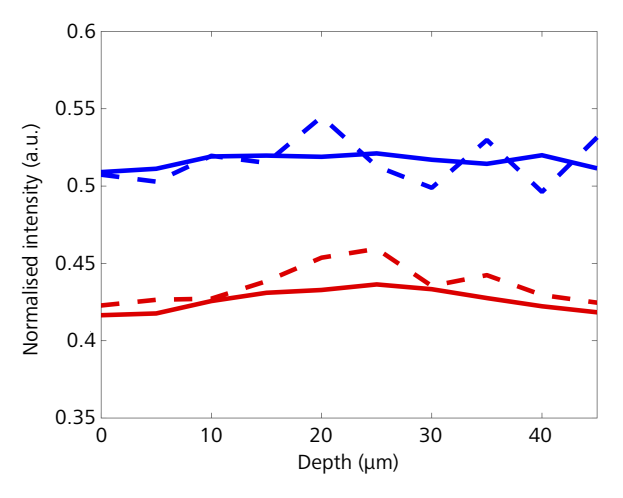
5.3 Elastography problem in the human retina

Understanding the mechanical properties of ocular tissues is essential in the diagnosis of retinal and corneal pathologies. Optical coherence elastography (OCE) is a promising imaging technique that combines high-resolution structural imaging with mechanical characterisation, providing valuable insights into tissue elasticity [23]. There are different implementations of OCE, varying in the type of mechanical loading of the tissue. Using a piezoelectric actuator to induce tissue displacements is one of many possible techniques.

In OCE, waves from a source propagate through the eye, including the cornea, the lens, and the vitreous humour, to reach the retina (see Figure 1). When the acoustic pressure interacts with the retina, it generates an elastic wave within the tissue. This elastic wave then propagates through the retina, potentially causing measurable displacements and providing information about the mechanical properties of the tissue. By analysing how tissues respond to acoustic excitations, it is possible to non-invasively infer variations of mechanical properties that often indicate disease. In particular, the response of the retina to these excitations is of primary clinical interest, and the accurate modelling of wave transmission



(a) DME group I has stronger intensity signal than the healthy controls.



(b) DME group II shows reduced signal compared to the healthy status.

Figure 8. Comparison between simulated A-scans (solid lines) and real A-scans, both normalised, for healthy controls (blue) and DME patients (red) [9].

through the anterior layers is essential for a correct interpretation. An accurate interpretation of the measured displacements requires a reliable numerical simulation of the wave propagation through layered, curved, and heterogeneous ocular structures.

In [6], the eye is described as a narrow cylindrical layered domain, where each layer Ω_j , j=1,...,n, represents a different ocular medium with distinct acoustic or elastic properties. The upper layer Ω_n corresponds to the retina and is modelled using an elastic wave equation, and the other layers are governed by acoustic wave propagation.

For the case of a piezoelectric actuator, electromagnetic fields induce mechanical displacements. When considering a time-harmonic emission in the source, the governing PDEs simplify significantly.

Let us now consider the mechanical deformation induced by the piezoelectric actuator, via the piezoelectric coupling

$$-\omega^2 \rho \mathbf{u} = \nabla \cdot (\mathbf{c} \cdot \mathbf{S} - \mathbf{e}^{\mathsf{T}} \cdot \mathbf{E}),$$

where ω denotes the frequency of the wave, ρ is the density of the medium, \mathbf{u} denotes the mechanical displacement, \mathbf{c} is the stiffness tensor, $\mathbf{S} = \frac{1}{2}(\nabla \mathbf{u} + \nabla \mathbf{u}^{\mathsf{T}})$ is the strain tensor, and \mathbf{e} is the piezoelectric coupling tensor.

The time-harmonic acoustic pressure p_j in the layer Ω_j satisfies the Helmholtz equation

$$\Delta p_j + k_j^2 p_j = 0$$
, in Ω_j , $j = 1, ..., n - 1$,

where $k_j = \omega/c_j$ is the wavenumber, dependent on the frequency ω and wave speed c_j in the layer Ω_j . For the first interface, $\partial\Omega_0$, one prescribes the boundary condition

$$\frac{1}{\rho_1} \frac{\partial p_1}{\partial \nu} = \omega^2 \mathbf{u} \cdot \nu_1, \quad \text{on } \partial \Omega_0.$$

Between layers, one prescribes the relations

$$p_j = p_{j+1}$$
, on $\partial \Omega_j$, $\rho_j \frac{\partial p_j}{\partial v_j} = \rho_{j+1} \frac{\partial p_{j+1}}{\partial v_{j+1}}$, on $\partial \Omega_j$,

where ρ_j is the density of the layer Ω_j and v_j is the outward unit normal to $\partial \Omega_j$.

The Lamé equation describes the elastic displacement field **u** in the retina:

$$\mu \Delta \mathbf{u} + (\lambda + \mu) \nabla (\nabla \cdot \mathbf{u}) + \omega^2 \rho \mathbf{u} = 0$$
, in Ω_n

where ρ denote the density in the retina, and the Lamé constants are given by

$$\mu = \frac{E}{2(1+v)}, \qquad \lambda = \frac{vE}{(1+v)(1-2v)},$$

with E the Young modulus and v the Poisson's ratio. The acousticelastic transmission condition is given by

$$\frac{1}{\rho_n}\frac{\partial p_{n-1}}{\partial \nu_n}=\omega^2\mathbf{u}\cdot \nu_n,\quad \text{on }\partial\Omega_{n-1},$$

$$p_{n-1}v_{n-1} = \sigma(\mathbf{u})v_n$$
, on $\partial \Omega_{n-1}$,

where the stress tensor is given by

$$\sigma(\mathbf{u}) = \mu(\nabla \mathbf{u} + (\nabla \mathbf{u})^{\mathsf{T}}) + \lambda \nabla \cdot \mathbf{u}I.$$

In [6], the method of fundamental solutions (MFS) was employed to approximate the solution in each layer, assuming homogeneity in each layer. The method was tested using physical parameters representative for the human eye and the application of the MFS to simulate the process of elastography seems feasible, even in the presence of high frequencies.

For the case of heterogeneous layers, the MFS is no longer suitable (because the fundamental solutions are not available) and the use of other types of methods, such as the DG method, is required.

Although layered models with planar interfaces simplify the geometry, real biological structures, such as the cornea and retina, have curved geometries. To obtain a model that closely resembles a real scenario, it is essential to capture these anatomical features. However, dealing with domains with curved boundary presents additional numerical challenges. It is well known that meshing curved domains using polygonal elements introduces geometric mismatches along the boundary. This discrepancy between $\partial\Omega$ and $\partial\Omega_h$ can significantly reduce the accuracy of numerical schemes. In particular, standard finite element or discontinuous Galerkin methods will be at most second-order accurate, regardless of the polynomial degree used for the numerical solution, unless specialised techniques are employed to recover the optimal rate.

To address this issue, we propose a method called DG-ROD (reconstruction for off-site data), presented in [26]. This approach is based on specific polynomial reconstructions constrained for the prescribed boundary conditions on the physical boundary $\partial\Omega$. The method recovers the optimal order of convergence of the DG method without relying on curved meshes to approximate the physical domain Ω . The overall DG-ROD method is based on an iterative procedure that alternates between a classical DG solver and a polynomial reconstruction step. In each iteration, a polynomial reconstruction is performed to improve the accuracy of the solution near the curved boundary. More specifically, for each boundary element, a new polynomial is computed such that it is the closest polynomial to the numerical DG solution on the computational domain, and the new polynomial exactly satisfies the prescribed boundary condition at a set of R points on the physical boundary. This new polynomial is then used to correct the boundary condition imposed on the computational polygonal boundary. The process is repeated until convergence is achieved.

To illustrate the ideas and validate the approach, consider the 2D Helmholtz equation $\Delta u + k^2 u = 0$ on a curved strip domain given by

$$\Omega = \{(x, y) : -1 < x < 1, h_2(x) < y < h_1(x)\},\$$

such that the solution satisfies a Neumann condition on the upper and lower parts of the boundary and a Dirichlet condition on the left and right parts of the boundary. In this benchmark, we take $h_1(x) = \sqrt{1+2\log(\cosh(x))}$ and $h_2(x) = h_1(x) - 0.2$. Consider the fundamental solution for the Helmholtz operator, with k=1, which is given by the Hankel function in 2D, $u(r) = \frac{i}{4}H_0^{(1)}(r)$, with r=|x| and i the imaginary unit [1]. Simulations are carried out with successively finer meshes generated by Gmsh (version 4.6.0) [13] (see Figure 9). The fixed point iterative procedure for the DG-ROD method stops when either the tolerance for the residual or the maximum number of iterations is reached. In order to determine the set of points used in the polynomial reconstructions, we consider the vertical projection of the nodal points located on the upper and lower computational boundaries onto the physical boundary.

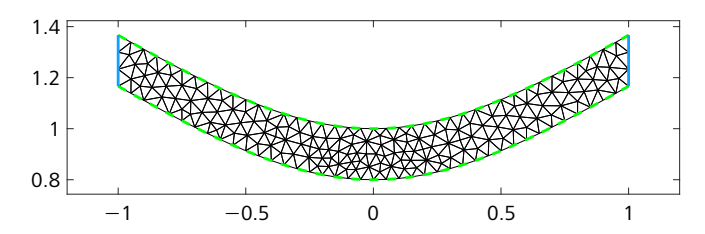


Figure 9. Unstructured mesh generated for the curved strip domain with Dirichlet (blue solid line) and Neumann boundary conditions (green dashed line).

Let u be the exact solution and u_h be the DG solution for a given mesh \mathcal{T}_h , and let $E_2(\mathcal{T}_h) = \|u - u_h\|_{L^2(\mathcal{T}_h)}$ be the L^2 -norm of the error. The method has order of convergence p if asymptotically

$$E_2(\mathcal{T}_h) \leq Ch^p$$

with C a real constant independent of h. The L^2 -errors are assessed at the node points of the elements of the mesh. Let \mathcal{T}_{h_1} and \mathcal{T}_{h_2} be two different meshes, with different mesh sizes h_1 and h_2 , respectively. Then, the order of convergence between two successively finer meshes is determined as

$$O_2(\mathcal{T}_{h_1}, \mathcal{T}_{h_2}) = \frac{\log(E_2(\mathcal{T}_{h_1})/E_2(\mathcal{T}_{h_2}))}{\log(h_1/h_2)}.$$

Note that each node on the computational boundary has a corresponding node on the real boundary where the boundary condition is prescribed. For the classical DG method, the value evaluated at the physical boundary point is used at the corresponding node on the computational boundary. The results for the classical DG method, reported in Table 2, demonstrate the deterioration of accuracy from the geometrical mismatch without any specific treatment for curved boundaries, and the error convergence is limited to the second-order. On the other hand, Table 3 reports the errors and convergence orders for the DG-ROD method. As observed, the convergence orders improve according to the polynomial degree N and the number of points used in the polynomial reconstruction in each element with a boundary edge. More precisely, this improvement occurs when the relation R = N + 1 is satisfied.

6 Conclusion

This review surveys a computational framework for modelling light propagation in the human eye using Maxwell's equations. The study addressed how structural changes in the cornea and retina influence light scattering and transparency, which are crucial for vision quality. Case studies explored clinically relevant scenarios, including corneal opacity, diabetic macular edema, and retinal elasticity. In each case, the numerical simulations provided insight into the structural changes, thereby facilitating early diagnosis.

К	h			N = 3			
		E ₂	02	E ₂	02	E ₂	<i>O</i> ₂
20	2.69E-01	9.79E-05	-	1.20E-04	-	1.26E-04	-
80	1.46E-01	2.55E-05	2.2	2.78E-05	2.4	2.85E-05	2.4
342	7.51E-02	6.42E-04	2.1	6.72E-06	2.1	6.79E-06	2.2
1454	3.94E-02	1.61E-06	2.1	1.65E-06	2.2	1.65E-06	2.2
5966	2.06E-02	4.02E-07	2.1	4.07E-07	2.2	4.08E-07	2.2

Table 2. Errors and convergence orders for the classical DG method in the curved strip domain.

К	h	N = 2, R = 3		N = 3, R = 4		N = 4, R = 5	
		E ₂	02	E ₂	02	E ₂	<i>O</i> ₂
20	2.69E-01	1.65E-04	-	2.85E-07	-	5.41E-08	-
80	1.46E-01	3.82E-05	2.4	3.81E-08	3.3	2.60E-09	5.0
342	7.51E-02	4.23E-06	3.3	2.31E-09	4.2	5.70E-11	5.8
1454	3.94E-02	8.31E-07	2.5	1.24E-10	4.5	-	-
5966	2.06E-02	1.79E-07	2.4	-	-	-	-

Table 3. Errors and convergence orders for the DG-ROD method in the curved strip domain.

Domains with curved boundary arise naturally in this problem setting due to the geometry of optical structures, such as the cornea and retina, which exhibit a curved layered composition. It is well known that curved domains require an accurate boundary representation to avoid a reduction of the order of convergence of numerical schemes. We considered a high-order discontinuous Galerkin method combined with a polynomial reconstruction technique. This approach enables an appropriate enforcement of boundary conditions without relying on curved meshes, preserving both computational efficiency and high-order accuracy.

Integrating accurate physical models with high-order numerical methods is a promising approach to simulate light propagation in the human eye. Future work will involve applying the method to curved interfaces within a layered medium in order to mimic the anatomy of the eye.

Acknowledgements. The authors acknowledge the financial support by FCT – Fundação para a Ciência e a Tecnologia, I. P., under the scope of the project UID/00324: Centro de Matemática da Universidade de Coimbra. Milene Santos was supported by FCT by project reference UI/BD/153816/2022.²

² https://doi.org/10.54499/UI/BD/153816/2022

- C. J. S. Alves and P. R. S. Antunes, Wave scattering problems in exterior domains with the method of fundamental solutions. *Numer. Math.* 156, 375–394 (2024)
- [2] A. Araújo, S. Barbeiro, R. Bernardes, M. Morgado and S. Sakić, A mathematical model for the corneal transparency problem. J. Math. Ind. 12, article no. 10 (2022)
- [3] A. Araújo, S. Barbeiro and M. K. Ghalati, Stability of a leap-frog discontinuous Galerkin method for time-domain Maxwell's equations in anisotropic materials. *Commun. Comput. Phys.* 21, 1350–1375 (2017)
- [4] A. Araújo, S. Barbeiro and M. K. Ghalati, Convergence of an explicit iterative leap-frog discontinuous Galerkin method for time-domain Maxwell's equations in anisotropic materials. J. Math. Ind. 8, article no. 9 (2018)
- [5] A. Araújo and S. Sakić, Stability and convergence of a class of RKDG methods for Maxwell's equations. In *Progress in industrial* mathematics at ECMI 2021, Math. Ind. 39, Springer, Cham, 493–499 (2022)
- [6] S. Barbeiro and P. Serranho, The method of fundamental solutions for the direct elastography problem in the human retina. In Advances in Trefftz methods and their applications, SEMA SIMAI Springer Ser. 23, Springer, Cham, 87–101 (2020)
- [7] R. Bernardes, A. Correia, O. C. d'Almeida, S. Batista, L. Sousa and M. Castelo-Branco, Optical properties of the human retina as a window into systemic and brain diseases. *Invest. Ophthalmol. Vis. Sci.* 55, article no. 3367 (2014)
- [8] T. A. Ciulla, A. G. Amador and B. Zinman, Diabetic retinopathy and diabetic macular edema: pathophysiology, screening, and novel therapies. *Diabetes Care* 26, 2653–2664 (2003)
- [9] A. Correia, L. Pinto, A. Araújo, S. Barbeiro, F. Caramelo, P. Menezes, M. Morgado, P. Serranho and R. Bernardes, Monte Carlo simulation of diabetic macular edema changes on optical coherence tomography data. *Proc. IEEE-EMBS Int. Conf. Biomed. Health Inform.* (BHI), 724–727 (2014)
- [10] J. Cunha-Vaz and R. Bernardes, Nonproliferative retinopathy in diabetes type 2. Initial stages and characterization of phenotypes. *Prog. Retin. Eye Res.* 24, 355–377 (2005)
- [11] A. Dunn and R. Richards-Kortum, Three-dimensional computation of light scattering from cells. *IEEE J. Sel. Top. Quantum Electron.* 2, 898–905 (1996)
- [12] J. Fujimoto and E. Swanson, The development, commercialization, and impact of optical coherence tomography. *Invest. Ophthalmol. Vis. Sci.* 57, OCT1–OCT13 (2016)
- [13] C. Geuzaine and J.-F. Remacle, Gmsh: A 3-D finite element mesh generator with built-in pre- and post-processing facilities. *Internat. J. Numer. Methods Engrg.* 79, 1309–1331 (2009)
- [14] J. S. Hesthaven and T. Warburton, Nodal discontinuous Galerkin methods: Algorithms, analysis, and applications. Texts Appl. Math. 54, Springer, New York (2008)

- [15] D. Huang, E. A. Swanson, C. P. Lin, J. S. Schuman, W. G. Stinson, W. Chang, M. R. Hee, T. Flotte, K. Gregory, C. A. Puliafito and J. G. Fujimoto, Optical coherence tomography. *Science* 254, 1178–1181 (1991)
- [16] International Diabetes Federation (IDF), IDF Diabetes Atlas Europe. (2024) https://idf.org/europe/our-network/our-members/
- [17] S. L. Jacques, Optical properties of biological tissues: a review. Phys. Med. Biol. 58, R37–R61 (2013)
- [18] J.-M. Jin, *Theory and computation of electromagnetic fields*. John Wiley & Sons, Hoboken, NJ; IEEE Press, New York (2010)
- [19] M. König, K. Busch, and J. Niegemann, The discontinuous Galerkin time-domain method for Maxwell's equations with anisotropic materials. *Photonics Nanostruct. Fundam. Appl.* 8, 303–309 (2010)
- [20] D. M. Maurice, The structure and transparency of the cornea. J. Physiol. 136, 263–286 (1957)
- [21] K. M. Meek and C. Knupp, Corneal structure and transparency. *Prog. Retin. Eye Res.* 49, 1–16 (2015)
- [22] J. Niegemann, R. Diehl and K. Busch, Efficient low-storage Runge– Kutta schemes with optimized stability regions. J. Comput. Phys. 231, 364–372 (2012)
- [23] Y. Qu, Y. He, Y. Zhang, T. Ma, J. Zhu, Y. Miao, C. Dai, M. Humayun, Q. Zhou and Z. Chen, Quantified elasticity mapping of retinal layers using synchronized acoustic radiation force optical coherence elastography. *Biomed. Opt. Express* 9, 4054–4063 (2018)
- [24] S. Saidha, O. Al-Louzi, J. N. Ratchford, P. Bhargava, J. Oh, S. D. Newsome, J. L. Prince, D. Pham, S. Roy, P. van Zijl, L. J. Balcer, E. M. Frohman, D. S. Reich, C. Crainiceanu and P. A. Calabresi, Optical coherence tomography reflects brain atrophy in multiple sclerosis: A four-year study. *Ann. Neurol.* 78, 801–813 (2015)
- [25] M. Santos, A. Araújo, S. Barbeiro, F. Caramelo, A. Correia, M. I. Marques, M. Morgado, L. Pinto, P. Serranho and R. Bernardes, Maxwell's equations based 3D model of light scattering in the retina. In 2015 IEEE 4th Portuguese Meeting on Bioengineering (ENBENG), 1–5 (2015)
- [26] M. Santos, A. Araújo, S. Barbeiro, S. Clain, R. Costa and G. J. Machado, Very high-order accurate discontinuous Galerkin method for curved boundaries with polygonal meshes. J. Sci. Comput. 100, article no. 66 (2024)
- [27] T. Santos, L. Ribeiro, C. Lobo, R. Bernardes and P. Serranho, Validation of the automatic identification of eyes with diabetic retinopathy by OCT. In 2012 IEEE 2nd Portuguese Meeting in Bioengineering (ENBENG), 1–4 (2012)
- [28] J. M. Schmitt, A. Knüttel and R. F. Bonner, Measurement of opticalproperties of biological tissues by low-coherence reflectometry. *Appl. Opt.* 32, 6032–6042 (1993)
- [29] P. Serranho, A. M. Morgado and R. Bernardes, Optical coherence tomography: a concept review. In Optical coherence tomography: A clinical and technical update, pp. 139–156, Springer, Berlin, Heidelberg (2012)
- [30] X. T. Su, K. Singh, W. Rozmus, C. Backhouse and C. Capjack, Light scattering characterization of mitochondrial aggregation in single cells. Opt. Express 17, 13381–13388 (2009)
- [31] J. H. Williamson, Low-storage Runge–Kutta schemes. J. Comput. Phys. 35, 48–56 (1980)

- [32] World Health Organization (WHO), Diabetes in the WHO European Region. (2024) https://www.who.int/europe/health-topics/diabetes
- [33] Y. L. Xu, Electromagnetic scattering by an aggregate of spheres. *Appl. Opt.* **34**, 4573–4588 (1995)

Adérito Araújo is an associate professor in the Department of Mathematics and a member of the Numerical Analysis and Optimization group at the Centre for Mathematics of the University of Coimbra. He has held leadership roles in several scientific organisations, including as president of the European Consortium for Mathematics in Industry (ECMI) from 2018 to 2020. His research focuses on mathematical modelling and numerical methods for biomedical applications, in collaboration with experts from diverse fields. He is currently editor-in-chief of the Journal of Mathematics in Industry and serves on the executive boards of both ECMI and EU-MATHS-IN (European Service Network of Mathematics for Industry and Innovation).

alma@mat.uc.pt

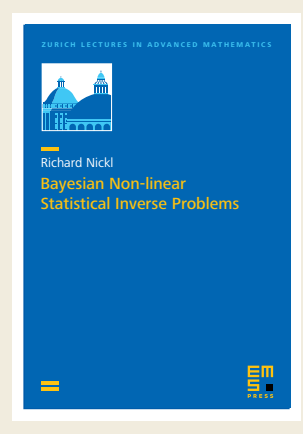
Sílvia Barbeiro is an associate professor in the Department of Mathematics and a member of the Numerical Analysis and Optimization group at the Centre for Mathematics of the University of Coimbra. Her research focuses on numerical analysis and computational mathematics, especially modelling and developing numerical methods for partial differential equations and machine learning techniques for inverse problems. Her work spans theoretical and applied aspects, with emphasis on biomathematics, engineering, geosciences, and medical imaging. In 2010, she received the L'Oréal Portugal Medal of Honour for Women in Science. She currently chairs the EMS Topical Activity Group on Mathematical Modelling in Life Sciences.

silvia@mat.uc.pt

Milene Santos is a PhD student in the Department of Mathematics and a member of the Numerical Analysis and Optimization group at the Centre for Mathematics of the University of Coimbra. She is currently working on discontinuous Galerkin methods for domains with curved boundary and their application in modelling light propagation in the human cornea.

milene@mat.uc.pt

EMS Press title



Bayesian Non-linear Statistical Inverse Problems

Richard Nickl (University of Cambridge)

Zurich Lectures in Advanced Mathematics

ISBN 978-3-98547-053-2 eISBN 978-3-98547-553-7

2023. Softcover. 171 pages. €39.00*

The present book presents a rigorous mathematical analysis of the statistical performance, and algorithmic complexity, of Bayesian methods based on Gaussian process priors in a natural setting of non-linear random design regression.

Due to the non-linearity present in many of these inverse problems, natural least squares functionals are non-convex and the Bayesian paradigm presents an attractive alternative to optimisation-based approaches. This book develops a general theory of Bayesian inference for non-linear forward maps and rigorously considers two PDE model examples arising with Darcy's problem and a Schrödinger equation. The focus is initially on statistical consistency of Gaussian process methods, and then moves on to study local fluctuations and approximations of posterior distributions by Gaussian or log-concave measures whose curvature is described by PDE mapping properties of underlying 'information operators'. Applications to the algorithmic runtime of gradient-based MCMC methods are discussed as well as computation time lower bounds for worst case performance of some algorithms.

*20% discount on any book purchases for individual members of the EMS, member societies or societies with a reciprocity agreement when ordering directly from EMS Press.

EMS Press is an imprint of the European Mathematical Society – EMS – Publishing House GmbH Straße des 17. Juni 136 | 10623 Berlin | Germany https://ems.press | orders@ems.press



ADVERTISEMENT